Relating pore shape to the non-linear response of periodic elastomeric structures

Johannes T.B. Overvelde [a], Katia Bertoldi [a,b,*]

[a] School of Engineering and Applied Sciences, Harvard University, Cambridge, MA 02138, USA
[b] Kavli Institute for Bianano Science and Technology, Harvard University, Cambridge, MA 02138, USA

ARTICLE INFO

ABSTRACT

By introducing a periodic array of pores in an elastic matrix, instabilities with wavelengths that are of the order of the size of the microstructure can be triggered. Interestingly, these instabilities can be utilized to design a novel class of responsive materials. Possible applications include materials with unusual properties such as negative Poisson's ratio, phononic and photonic switches and colorful and reconfigurable displays.

Although shape plays an important role in the design and performance of periodic materials, so far only the non-linear response of structures with circular and elliptical pores has been investigated and the effect of the pore shape on the structural response has not yet been explored. Here, we numerically explore the effect of pore shape on the non-linear response of a square array of pores in an elastomeric matrix. Our results show that pore shape can be used effectively to design material with desired properties and to control attractive features of soft porous systems, such as their stiffness, critical strain and negative Poisson's ratio.
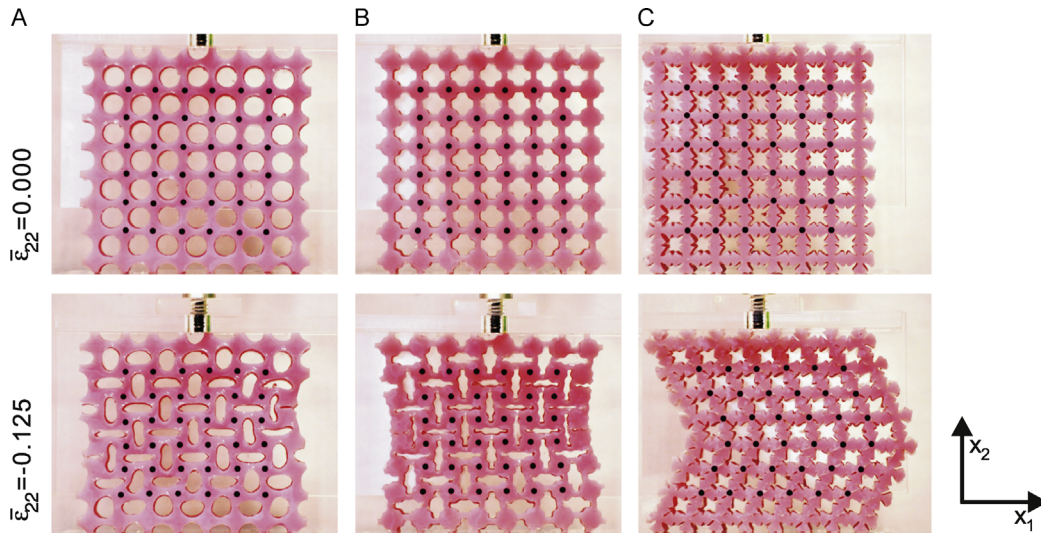
© 2013 Elsevier Ltd. All rights reserved.

1. Introduction

Materials with significant porosity, generally termed cellular solids, exhibit properties that differ from those of their solid counterparts and have a large number of uses in mechanical and thermal applications (Gibson and Ashby, 1999; Wadley, 2006). In particular, cellular solids are used to design lightweight structures (Queheillalt and Wadley, 2005), to maximize energy absorption (Wierzbicki and Abramowicz, 1983; Papka and Kyriakides, 1994) and for acoustic damping (Verdejo et al., 2009). The connections between the architecture of such materials and their macroscopic properties have been investigated by many researchers (Gibson and Ashby, 1999; Wadley, 2006; Evans et al., 2001; Ashby and Bréchet, 2003). Moreover, the non-linear stress–strain behavior of cellular solids has been of particular interest (Gibson and Ashby, 1999; Papka and Kyriakides, 1998; Triantafyllidis and Schraad, 1998; Ohno et al., 2002; Tantikom et al., 2005; Chung and Waas, 2002). Under compression, elastic foams deform linearly to a strain of about 5%. Then, their cell walls buckle and they collapse at a nearly constant stress until contact between cell walls occurs, giving rise to the final steep portion of the stress–strain curve. Polymeric and metallic foams have similar stress–strain curves, but after instability they deform plastically at nearly constant stress until the cell walls touch.

Although traditionally instabilities have been viewed as an inconvenience, buckling need not to be deleterious: buckling plays an important role in the morphogenesis of some plant parts (Steele, 2000); the surface pattern of a dehydrated fruit is dominated by buckling (Yin et al., 2008) and buckling caused by swelling increases the leave motility in the Venus flytrap (Forterre et al., 2005). Inspired by nature, researchers have recently demonstrated instabilities to be instrumental in controlling adhesion (Chan et al., 2008), facilitating flexible electronics (Rogers et al., 2010), fabricating micro-fluidic structures (Khare et al., 2009), controlling surface wettability (Chung et al., 2007), providing means for micro- and nano-patterning and

---

* Corresponding author.
  E-mail address: bertoldi@seas.harvard.edu (K. Bertoldi).

ARTICLE IN PRESS

2   J.T.B. Overvelde, K. Bertoldi / J. Mech. Phys. Solids ▮ (▮▮▮▮) ▮▮▮–▮▮▮

Fig. 1. Experimental images of three periodic structures with differently shaped pores loaded under uniaxial compression (Overvelde et al., 2012). All structures are characterized by 50% porosity and the engineering strain $\varepsilon_{22} = -0.125$ is applied. The shape of the pores is found to strongly affect the instability. In structures A and B the critical instability is characterized by a short wavelength and leads to the formation of a checkerboard pattern. In contrast, a buckling mode with a wavelength equal to the size of the sample is observed in structure C, reminiscent of the twinning observed in austenite to martensite phase transformations in shape memory alloys.

designing optical micro-devices (Yoo et al., 2002; Zhang et al., 2008), designing active micro-hydrogel devices (Lee et al., 2010) and reversible encapsulation systems (Shim et al., 2012).

2D periodic porous structures recently attracted considerable interest because of the dramatic transformations of the original geometry that may be observed as the result of mechanical instabilities. Upon reaching a critical applied deformation, a square array of circular pores in an elastomeric matrix is found to suddenly transform into a periodic pattern of alternating, mutually orthogonal ellipses (Michel et al., 2007; Mullin et al., 2007; Bertoldi et al., 2008; Zhang et al., 2008). Remarkably, it has been demonstrated that these instabilities provide opportunities for fabrication of complex microstructures (Zhang et al., 2008) and for the design of materials with unusual properties such as negative Poisson's ratio (Bertoldi et al., 2010), phononic (Jang et al., 2009) and photonic switches (Krishnan and Johnson, 2009) and reprogrammable colorful displays (Li et al., 2012).

Here, we focus on 2D elastomeric porous structures and investigate the effect of pore shape on their non-linear behavior. While it has been recently shown that the pore arrangement (Triantafyllidis et al., 2006; Michel et al., 2007; Shim et al., 2013), the porosity of the solid (Bertoldi et al., 2010) and the loading conditions (Michel et al., 2007) have a strong effect on the stability of the system, the goal of this work is to provide a deep understanding in the effect of pore shape on the global response of the structure. Since it has been recently demonstrated that pore shape has a strong effect on the instability, affecting not only the point where instability occurs, but also its wavelength (Overvelde et al., 2012) (see Fig. 1), we conduct a systematic numerical study to identify the effect of pore shape on the non-linear response of the periodic elastomeric structures, while keeping the porosity, hole arrangement and loading conditions fixed.

The pore shape is found to provide a convenient parameter to control not only the initial stiffness and the critical strain, but also attractive features of soft porous systems, such as their negative Poisson's ratio.[1] Our results show that the pore shape can be used effectively to design material with desired properties and pave the way for the development of a new class of soft, active and reconfigurable devices over a wide range of length scales.
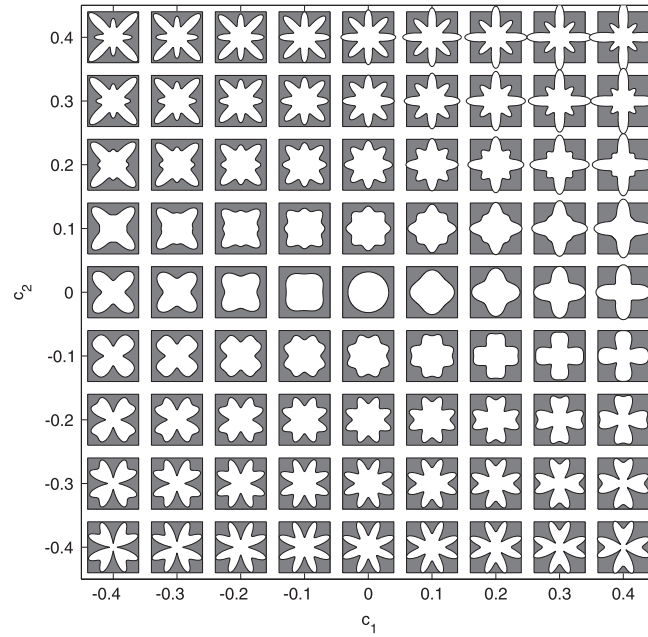
The paper is organized as follows. First, the family of pore shapes investigated in this study is presented in Section 2. Then, in Section 3 the numerical analyses that are used to investigate the non-linear response of infinite periodic and porous structures are introduced. Finally, numerical results are presented and discussed in Section 4, highlighting the effect of the pore shape on the macroscopic response of the periodic elastomeric structures.
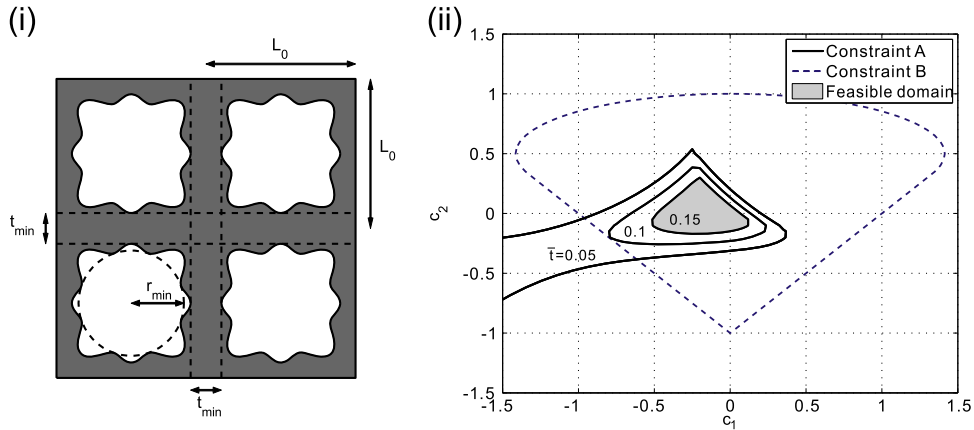
2. Microstructure

In this study, we consider a square array of pores in an elastomeric matrix and focus on pores with four-fold symmetry. Taking the circular pore shape as a starting point, we make use of Fourier series expansion to alter their contour according to

$$x_1 = r(\theta) \cos\,\theta, \quad x_2 = r(\theta) \sin\,\theta,$$
$$\text{with } r(\theta) = r_0[1 + c_1 \,\cos\,(4\theta) + c_2\,\cos\,(8\theta)], \tag{1}$$

---

[1] Although Poisson's ratio is rigorously defined in the framework of linear elasticity, here we extend the concept to finite elasticity and use it to quantify the lateral deformation of the material.

ARTICLE IN PRESS

J.T.B. Overvelde, K. Bertoldi / J. Mech. Phys. Solids ∎ (∎∎∎∎) ∎∎∎–∎∎∎   3

Fig. 2. Pore shapes obtained using Eq. (1) for $c_1 = c_2 = -0.4, 0.3, …, 0.4$ and $\phi_0 = 0.5$.

Fig. 3. (i) Schematic indicating t_{min}, L_0 and r_{min}, which are used in the constraints defined in Eqs. (3) and (4). (ii) *Constraint A* and *Constraint B* as a function of c_1 and c_2 for $\phi_0 = 0.5$ and $\bar{t} = 0.05, 0.1, 0.15$.

where $0 \leq \theta \leq 2\pi$ and three parameters have been introduced to control the pore size (r_0) and shape (c_1 and c_2). While $c_1 = c_2 = 0$ in Eq. (1) provides a description of a circle of radius r_0, by changing c_1 and c_2 a variety of shapes can be obtained, as shown in Fig. 2. Thus, in terms of shape optimization, c_1 and c_2 represent a 2D design space that allows for a systematic study of the effect of pore shape on the non-linear response of the periodic structures. Since we focus on pores arranged on a square array, r_0 is related to the initial porosity of the structure ϕ_0 through

$$r_0 = \frac{L_0 \sqrt{2\phi_0}}{\sqrt{\pi(2 + c_1^2 + c_2^2)}}, \tag{2}$$

with L_0 denoting the center-to-center distance between neighboring pores in the undeformed configuration, as specified in Fig. 3i.

Note that, to preserve the structural integrity the pair (c_1, c_2) has to be chosen such that

- *Constraint A*: a minimum distance between pore boundaries is preserved. Therefore, the minimum ligament thickness $t_{min} = L_0 - 2 \max(x_1)$ has to satisfy

$$\frac{t_{min}}{L_0} \geq \bar{t}, \tag{3}$$

ARTICLE IN PRESS

4   J.T.B. Overvelde, K. Bertoldi / J. Mech. Phys. Solids ∎ (∎∎∎∎) ∎∎∎–∎∎∎

$\bar{t}$ denoting the normalized minimum feature size in the structure.

- *Constraint B*: the minimum radius of the pore r_{min} is positive, i.e.

$$r_{min} = \min[r(\theta)] \geq 0, \tag{4}$$

$r(\theta)$ being defined in Eq. (1).

As it can be observed in Fig. 3ii, both *Constraint A* and *Constraint B* bound the feasible domain of pore shapes (i.e. area enclosed by the constraints boundary lines). The domain considered in this study is defined by $\phi_0 = 0.5$ and $\bar{t} = 0.15$ and it is highlighted in gray in Fig. 3ii.

3. Modeling

In this section, we will present the analyses that are used to investigate the non-linear response of infinite periodic structures. First, we will introduce the material model (see Section 3.1) and loading conditions (see Section 3.2). Then, we will focus on the analyses to detect the onset of microscopic or macroscopic instability (see Section 3.3). Finally, we will discuss the post-buckling analysis (see Section 3.4).

3.1. Material model

The response of the elastomeric material used to fabricate the structures in previous work (Overvelde et al., 2012) is captured using a Neo-Hookean model (Ogden, 1998). Let $\mathbf{F} = \partial\mathbf{x}/\partial\mathbf{X}$ be the deformation gradient, mapping a material point from the reference position $\mathbf{X}$ to its current location $\mathbf{x}$. Furthermore, let J be the determinant of $\mathbf{F}$, i.e. $J = \det \mathbf{F}$. In the absence of body forces, equilibrium of the body is ensured when the first Piola–Kirchoff stress $\mathbf{S}$ satisfies

$$\text{Div } \mathbf{S} = \mathbf{0}. \tag{5}$$

For a hyperelastic material, with a response described by the free-energy $W(\mathbf{F})$, the first Piola–Kirchoff stress is given by

$$\mathbf{S} = \frac{\partial W}{\partial \mathbf{F}}. \tag{6}$$

The strain energy density function of a Neo-Hookean material modified to include compressibility (with a high bulk modulus) is given by

$$W = \frac{\mu}{2}\left(J^{-2/3}I_1 - 3\right) + \frac{\kappa}{2}(J-1)^2, \tag{7}$$

where $\mu = E/[2(1+\nu)]$ and $\kappa = E/[3(1-2\nu)]$ denote the initial shear and bulk moduli, respectively, E and ν being the material's Young's modulus and Poisson's ratio and $I_1 = \text{tr}(\mathbf{F}\mathbf{F}^T)$. The first Piola–Kirchoff stress tensor is then obtained as

$$\mathbf{S} = \frac{\partial W}{\partial \mathbf{F}} = J^{-2/3}\mu\left[\mathbf{F} - \frac{1}{3}I_1\mathbf{F}^{-T}\right] + J\kappa(J-1)\mathbf{F}^{-T}. \tag{8}$$

3.2. Boundary conditions

Although the non-linear response of periodic structures can be numerically investigated on finite size structures, to reduce the size of the computational model we will focus on structures of infinite size. Furthermore, it is important to note that the response of infinite size structures is not influenced by boundary effects, hence facilitating the comparison of structures with different pore shapes. These infinite periodic structures can be modeled by considering a Representative Volume Element (RVE) and applying periodic boundary conditions.

In this study a stability analysis is first performed on an RVE comprising a single pore. Subsequently, RVEs with size dictated by the periodicity of the critical mode are constructed and their post-buckling response is investigated. Each RVE is subjected to a macroscopic deformation gradient imposing periodic boundary conditions, so that

$$\mathbf{u}_B - \mathbf{u}_A = (\bar{\mathbf{F}} - \mathbf{I})(\mathbf{X}_B - \mathbf{X}_A), \tag{9}$$

where A and B are two periodically located points on the boundary of the RVE and $\mathbf{u}_D = \mathbf{x}(\mathbf{X}_D) - \mathbf{X}_D$ denotes the displacement of node D. The macroscopic deformation can be imposed by prescribing the components of the macroscopic displacement gradient $(\bar{\mathbf{F}} - \mathbf{I})$, which are viewed as generalized degrees of freedom operationally applied using a set of virtual nodes (Danielsson et al., 2002). Rigid body motion is prevented by constraining the displacement of a single point. Note that in this paper we use an overbar to indicate macroscopic (i.e. homogenized) quantities.

ARTICLE IN PRESS

J.T.B. Overvelde, K. Bertoldi / J. Mech. Phys. Solids ∎ (∎∎∎∎) ∎∎∎–∎∎∎   5

In this study, uniaxial compression in the vertical direction under plane strain conditions is considered, so that

$$\overline{\mathbf{F}} = (1+\overline{\varepsilon}_{11})\mathbf{e}_1 \otimes \mathbf{e}_1 + (1+\overline{\varepsilon})\mathbf{e}_2 \otimes \mathbf{e}_2 + \mathbf{e}_3 \otimes \mathbf{e}_3. \tag{10}$$

$\overline{\varepsilon}$ denoting the applied vertical engineering strain and $\overline{\varepsilon}_{11}$ being such that $\overline{S}_{11} = 0$.

3.3. Instability analysis

When a periodic structure deforms, its spatial periodicity can abruptly change due to mechanical instability. The mechanics of incremental deformation superimposed upon a given state of finite deformation allows the investigation of instabilities that develop in an infinite porous solid. Let us consider a perturbation of the tractions applied to the undeformed configuration that takes the body to a new equilibrium configuration, in which the equations of motion are still satisfied. The incremental problem is governed by

$$\text{Div } \dot{\mathbf{S}} = \rho_0 \frac{D^2 \dot{\mathbf{x}}}{Dt^2}, \tag{11}$$

where $\dot{\mathbf{S}}$ denotes the incremental first Piola–Kirchhoff stress tensor and $\dot{\mathbf{x}}$ the incremental displacement field. Note that for a non-linear elastic material characterized by a stored-energy function W, $\dot{\mathbf{S}}$ is given by

$$\dot{S}_{ij} = \mathbb{L}_{ijkl}\dot{F}_{kl}, \quad \text{with } \mathbb{L}_{ijkl} = \frac{\partial W}{\partial F_{ij}\partial F_{kl}}. \tag{12}$$

For infinite periodic structures it is useful to make the distinction between *microscopic* instabilities (i.e. instabilities with wavelengths that are of the order of the size of the microstructure) and *macroscopic* instabilities (i.e. instabilities with much larger wavelengths in comparison to the size of the unit cell) (Geymonat et al., 1993; Triantafyllidis et al., 2006; Bertoldi et al., 2008; Overvelde et al., 2012).

3.3.1. Microscopic instabilities

Although microscopic instabilities may alter the initial periodicity of the solid, they can still be detected focusing on the primitive cell spanned by the lattice vectors $\mathbf{A}_1$ and $\mathbf{A}_2$ and investigating the propagation of small-amplitude elastic waves superimposed on a finite state of deformation (Geymonat et al., 1993; Triantafyllidis et al., 2006; Bertoldi et al., 2008)

$$\dot{\mathbf{x}}(\mathbf{X}, t) = \dot{\tilde{\mathbf{x}}} \exp(i\mathbf{K}_0 \cdot \mathbf{X} - i\omega t), \tag{13}$$

here ω and $\mathbf{K}_0$ are the angular frequency and wave vector of the propagating wave, respectively, and $\dot{\tilde{\mathbf{x}}}$ denotes the magnitude of the incremental displacement.

While a real angular frequency ω corresponds to a propagating wave, a complex angular frequency identifies a perturbation growing exponentially in time. Therefore, the transition between a stable and an unstable configuration, identified by the critical loading parameter $\overline{\varepsilon}_{cr}$, is detected when the frequency vanishes (i.e. $\omega = 0$). The new periodicity of the solid introduced by instability can then be obtained by the corresponding wave vector.

Therefore, to detect the onset of microscopic instabilities, we first load the primitive unit cell to a certain extent and then apply incremental displacements given by the Bloch-type relation to the boundary of the primitive cell

$$\dot{\mathbf{x}}_A = \dot{\mathbf{x}}_B \exp[i\mathbf{K}_0 \cdot \mathbf{R}_{AB}]\exp(-i\omega t), \tag{14}$$

A and B being two periodically located nodes on the primitive cell boundary and $\mathbf{R}_{AB}$ denoting the distance vector between these nodes in the undeformed configuration, i.e. $\mathbf{R}_{AB} = \mathbf{X}_B - \mathbf{X}_A$. A number of wave vectors are considered and for each of them the corresponding angular frequency ω is determined by solving the frequency domain equations

$$\text{Div } \dot{\tilde{\mathbf{S}}} = \rho_0 \, \omega^2 \dot{\tilde{\mathbf{x}}}, \tag{15}$$

with

$$\dot{\mathbf{S}}(\mathbf{X}, t) = \dot{\tilde{\mathbf{S}}}(\mathbf{X})\exp(-i\omega t). \tag{16}$$

A microscopic instability is detected at the first point along the loading path for which a wave vector $\mathbf{K}_{0,cr}$ exists such that the corresponding angular frequency ω is zero. Let us write $\mathbf{K}_{0,cr}$ as

$$\mathbf{K}_{0,cr} = K_{1,cr}\mathbf{B}_1 + K_{2,cr}\mathbf{B}_2, \tag{17}$$

where $\mathbf{B}_1$ and $\mathbf{B}_2$ denote the reciprocal lattice vectors

$$\mathbf{B}_1 = 2\pi \frac{\mathbf{A}_2 \times \mathbf{e}}{A}, \quad \mathbf{B}_2 = 2\pi \frac{\mathbf{e} \times \mathbf{A}_1}{A} \quad \text{with} \quad A = \|\mathbf{A}_1 \times \mathbf{A}_2\|, \quad \mathbf{e} = \frac{\mathbf{A}_1 \times \mathbf{A}_2}{A}, \tag{18}$$

$\mathbf{A}_1$ and $\mathbf{A}_2$ defining the lattice vectors which span the primitive cell. Then, the instability will result in a new RVE with $n_1 \times n_2$ primitive unit cells in the two directions spanned by the lattice vectors, where

$$n_1 = \frac{1}{K_{1,cr}}, \quad n_2 = \frac{1}{K_{2,cr}}. \tag{19}$$

ARTICLE IN PRESS

6   J.T.B. Overvelde, K. Bertoldi / J. Mech. Phys. Solids ∎ (∎∎∎∎) ∎∎∎–∎∎∎

Since commercial finite-element software packages normally do not support complex-valued displacements, following Aberg and Gudmundson (1997) all spatial fields ψ are split into a real and imaginary part

$$\psi(\mathbf{X}) = \psi^{\text{re}}(\mathbf{X}) + i\psi^{\text{im}}(\mathbf{X}), \tag{20}$$

so that the frequency-domain wave equations (15) split into

$$\text{Div } \dot{\mathbf{S}}^{\text{re}} = \rho_0 \omega^2 \dot{\mathbf{x}}^{\text{re}}, \quad \text{Div } \dot{\mathbf{S}}^{\text{im}} = \rho_0 \, \omega^2 \dot{\mathbf{x}}^{\text{im}}. \tag{21}$$

These two sets of equations can be solved simultaneously using two identical finite-element meshes for the primitive cell and coupling them by the incremental displacement boundary conditions from Eq. (14)

$$\dot{\mathbf{x}}_B^{\text{re}} = \dot{\mathbf{x}}_A^{\text{re}} \, \cos[i\mathbf{K}_0 \cdot \mathbf{R}_{AB}] - \dot{\mathbf{x}}_A^{\text{im}} \, \sin[i\mathbf{K}_0 \cdot \mathbf{R}_{AB}],$$
$$\dot{\mathbf{x}}_B^{\text{im}} = \dot{\mathbf{x}}_A^{\text{re}} \, \sin[i\mathbf{K}_0 \cdot \mathbf{R}_{AB}] + \dot{\mathbf{x}}_A^{\text{im}} \, \cos[i\mathbf{K}_0 \cdot \mathbf{R}_{AB}]. \tag{22}$$

3.3.2. Macroscopic instabilities

Macroscopic (or long wavelength) instabilities can be detected considering $\mathbf{K}_0 \rightarrow \mathbf{0}$ when performing the Bloch wave analysis described in the previous section. Alternatively, it has been rigorously shown that macroscopic instabilities can also be detected from the loss of strong ellipticity of the overall response of the material (Geymonat et al., 1993). Specifically, for the porous material considered in this study macroscopic instability may occur whenever the condition

$$\mathbb{L}_{ijkl}^H N_j N_l m_i m_k > 0 \quad \text{for} \quad \mathbf{m} \otimes \mathbf{N} \neq 0, \tag{23}$$

is first violated along the loading path, $\mathbf{m}$ and $\mathbf{N}$ denoting unit vectors. Note that $\mathbb{L}^H$ denotes the macroscopic (homogenized) tangent modulus of the solid that is evaluated numerically by subjecting the RVE to four independent linear perturbations of the macroscopic deformation gradient (Bertoldi et al., 2008).

3.4. Post-buckling analysis

For materials characterized by a critical microscopic buckling mode we investigate the non-linear post-buckling response. RVEs with size dictated by the critical periodicity $n_1 \times n_2$ identified through the Bloch Wave analysis are built and an imperfection in the form of the most critical buckling mode, ψ_{cr}, is introduced into the mesh. Therefore, the mesh is perturbed by ψ_{cr} scaled by a factor w, so that

$$w \max|\psi_{cr}| = 0.005 L_0, \tag{24}$$

where L_0 denotes the size of the primitive cell in the undeformed configuration.

Periodic boundary conditions (see Eq. (9)) are used and the RVEs are loaded according to Eq. (10) with compressive applied strain $\bar{\varepsilon}$ increased until the pores completely collapse. The evolution of both the macroscopic stress and the deformation of the microstructure is monitored during the simulations.
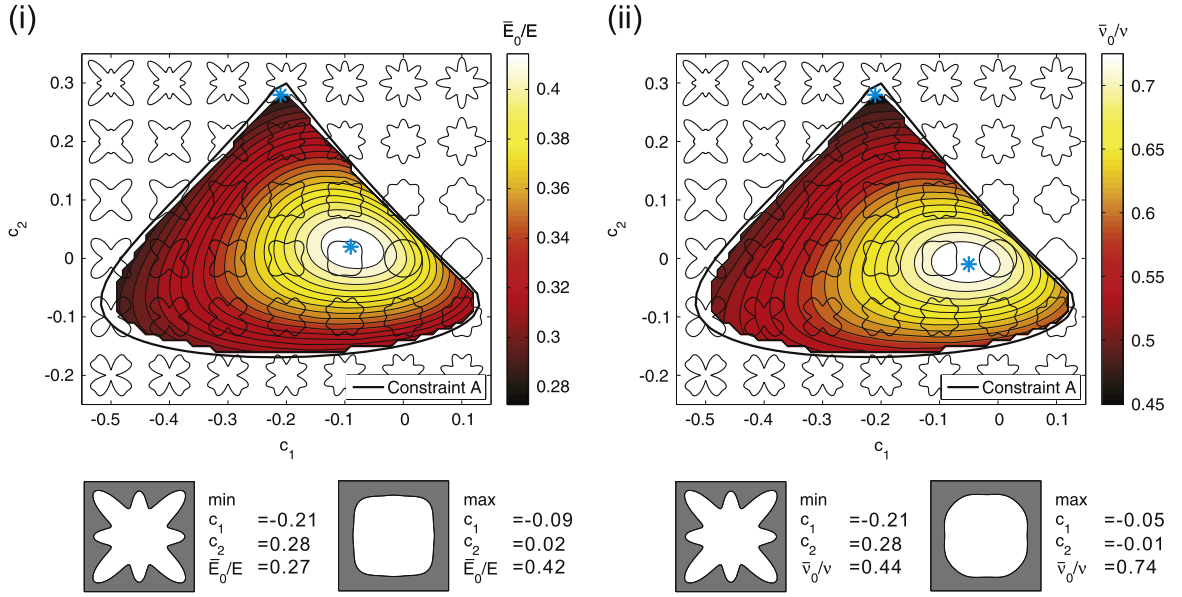
4. Results

In this study numerical simulations are performed to determine the effect of pore shape on the response of periodic elastomeric structures. First, the linear elastic response of the feasible structures is investigated (see Section 4.1). Then, the stability of the structures is studied, demonstrating that pore shape has a significant effect not only on the critical load, but also on the wavelength of the instability (see Section 4.2). Finally, since it has been recently shown that microscopic instabilities can be exploited to effectively tune the properties of the materials and to achieve unusual response such as negative Poisson's ratio (Bertoldi et al., 2010), we focus on the post-buckling response of structures for which short wavelength instabilities are critical (see Section 4.3). In particular, the effect of pore shape is highlighted by inspecting the evolution of stress, incremental stiffness and Poisson's ratio as a function of the applied loading.

The response of the porous structures is studied using the non-linear finite-element code ABAQUS/Standard. Triangular, quadratic, plane strain elements (ABAQUS element type CPE6H) were used and the accuracy of the mesh was ascertained through a mesh refinement study, resulting in a relative mesh density of around 800–1250 elements per primitive cell. To focus on the effect of pore shape, we limit ourselves to structures characterized by an initial porosity $\phi_0 = 0.5$ and a minimum wall thickness $\bar{t} = 0.15$ in *Constraint A*, as specified in Eq. (3). The feasible combinations of the pore shape parameters c_1 and c_2 for the structures considered in this study correspond to the area highlighted in gray in Fig. 3ii.

4.1. Initial response

We start by determining the initial response of the feasible structures. The initial response is determined by considering a primitive cell and applying a small uniaxial strain $\bar{\varepsilon} = 1 \times 10^{-4}$, which results in approximately linear behavior. Then, the

ARTICLE IN PRESS

J.T.B. Overvelde, K. Bertoldi / J. Mech. Phys. Solids ∎ (∎∎∎∎) ∎∎∎–∎∎∎   7

Fig. 4. (i) Contour map showing the initial macroscopic stiffness $\overline{E}_0/E$ as a function of c_1 and c_2. (ii) Contour map showing the initial macroscopic Poisson's ratio $\overline{\nu}_0/\nu$ as a function of c_1 and c_2.

initial stiffness $\overline{E}_0$ and Poisson's ratio $\overline{\nu}_0$ are calculated as

$$\overline{E}_0 = \left(\frac{\partial \overline{S}_{22}}{\partial \overline{\varepsilon}}\right)_{\overline{\varepsilon}=0} \quad \text{and} \quad \overline{\nu}_0 = -\left(\frac{\overline{\varepsilon}_{11}}{\overline{\varepsilon}}\right)_{\overline{\varepsilon}=0}, \tag{25}$$

where $\overline{S}_{22}$ denotes the uniaxial macroscopic stress.

Fig. 4i and ii show the dependence of $\overline{E}_0$ and $\overline{\nu}_0$ on c_1 and c_2 for all feasible structures. As expected, both the initial stiffness and Poisson's ratio of the porous structure are lower than the corresponding properties of the bulk material. Moreover, although the porosity ϕ_0 is equal for all structures, we note that the pore shape has a significant effect on the structural response. In particular, $\overline{E}_0/E$ and $\overline{\nu}_0/\nu$ vary continuously within the feasible domain specified by *Constraint A*, so that $0.28 \leq \overline{E}_0/E \leq 0.42$ and $0.45 \leq \overline{\nu}_0/\nu \leq 0.70$. Moreover, it is worth mentioning that the pore shape affects $\overline{E}_0$ and $\overline{\nu}_0$ in a very similar way. As a result, pores characterized by $(c_1, c_2) = (-0.21, 0.28)$ are found to lead to minimum values of both $\overline{E}_0$ and $\overline{\nu}_0$. In contrast, maximum values for $\overline{E}_0$ and $\overline{\nu}_0$ are attained for pores with an almost square shape.

To better understand the effect of pore shape on the initial response of the porous materials, in Fig. 5 we present the distribution of the nominal stress component S_{22} for nine representative structures. The images clearly show that the compressive load is fully carried by the vertical members. Therefore, an effective column with width w_{eff} can be defined, so that

$$\overline{E}_0 = \frac{Ew_{eff}}{L_0}. \tag{26}$$

In Fig. 5 vertical dashed lines are used to identify the effective column width, showing a very strong correlation between w_{eff} and the distribution of the stress within the structure. Furthermore, if we assume that the load is fully carried by vertical columns of width w_{eff}, the transverse strain $\overline{\varepsilon}_{11}$ for the porous structure can be approximated by

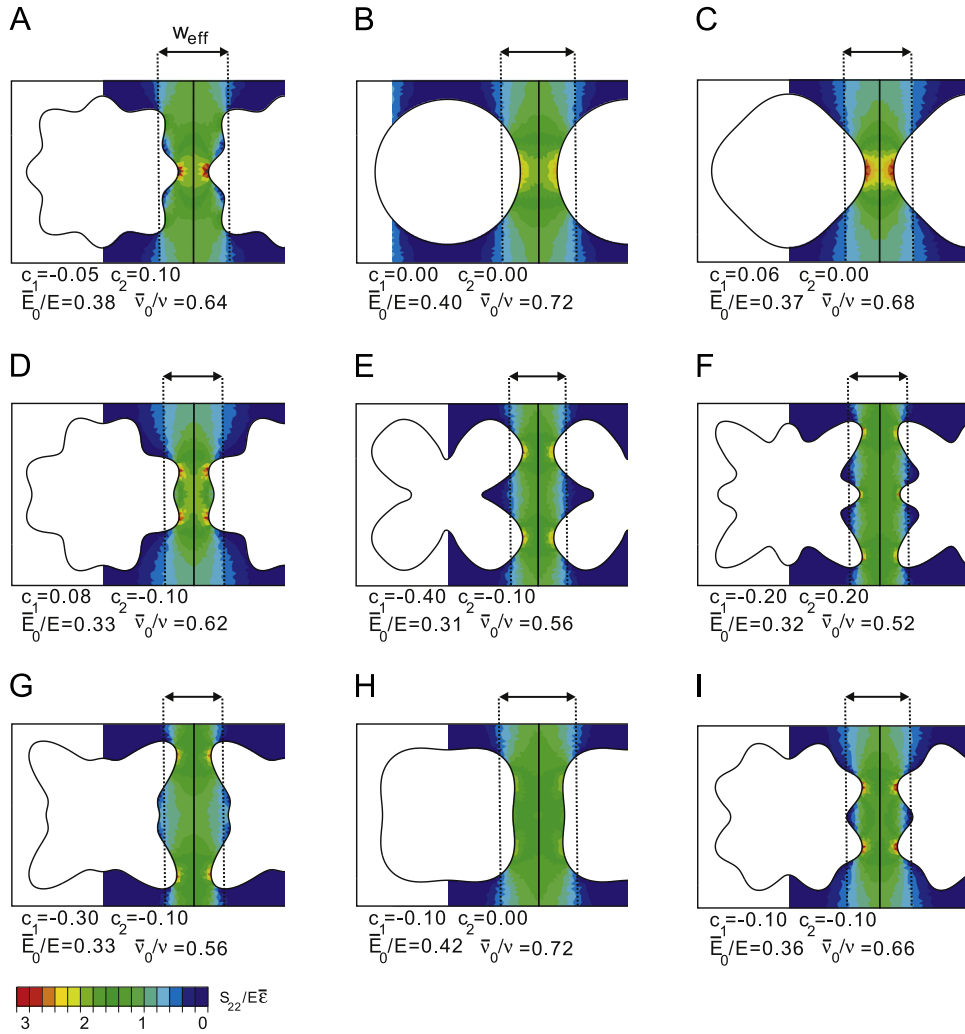$$\overline{\varepsilon}_{11} \approx -\frac{\overline{\varepsilon}\nu w_{eff}}{L_0}, \tag{27}$$

so that the macroscopic Poisson's ratio is given by

$$\overline{\nu}_0 = -\frac{\overline{\varepsilon}_{11}}{\overline{\varepsilon}} \approx \frac{\nu w_{eff}}{L_0}. \tag{28}$$

Comparison of Eqs. (26) and (28) clearly shows that our simple analysis predicts the same dependence of $\overline{E}_0$ and $\overline{\nu}_0$ on w_{eff}. Therefore, we expect the effect of pore shape on these two macroscopic properties to be the same. This prediction is confirmed by numerical results reported in Fig. 4.

4.2. Instability analysis

Here, we investigate the stability of the feasible structures under uniaxial compression. It has been recently shown that pore shape has a significant effect not only on the critical load, but also on the wavelength of the instability (Overvelde et al.,

Fig. 5. Distribution of the nominal stress component S_{22} for nine representative structures. The vertical dotted lines specify the effective width w_{eff} (see Eq. (26)).

2012). While the previous work only focused on three pore shapes, in this study we conduct an extensive numerical study on the effect of c_1 and c_2 on the non-linear response of the porous structures. We start by determining the critical strain at the onset of microscopic ($\bar{\varepsilon}_{cr}^{micro}$) and macroscopic ($\bar{\varepsilon}_{cr}^{macro}$) instability for all the pore shapes within the feasible $c_1 - c_2$ domain. To efficiently calculate the critical strains, we implement a discrete Newton–Raphson algorithm, so that the increment of the applied strain $\Delta\bar{\varepsilon}$ for each loading step is determined as

$$\Delta\bar{\varepsilon}^{i+1} = \Delta\bar{\varepsilon}^i + \left(\Delta\bar{\varepsilon}^i - \Delta\bar{\varepsilon}^{i-1}\right)\frac{f^i}{f^i - f^{i-1}}, \tag{29}$$
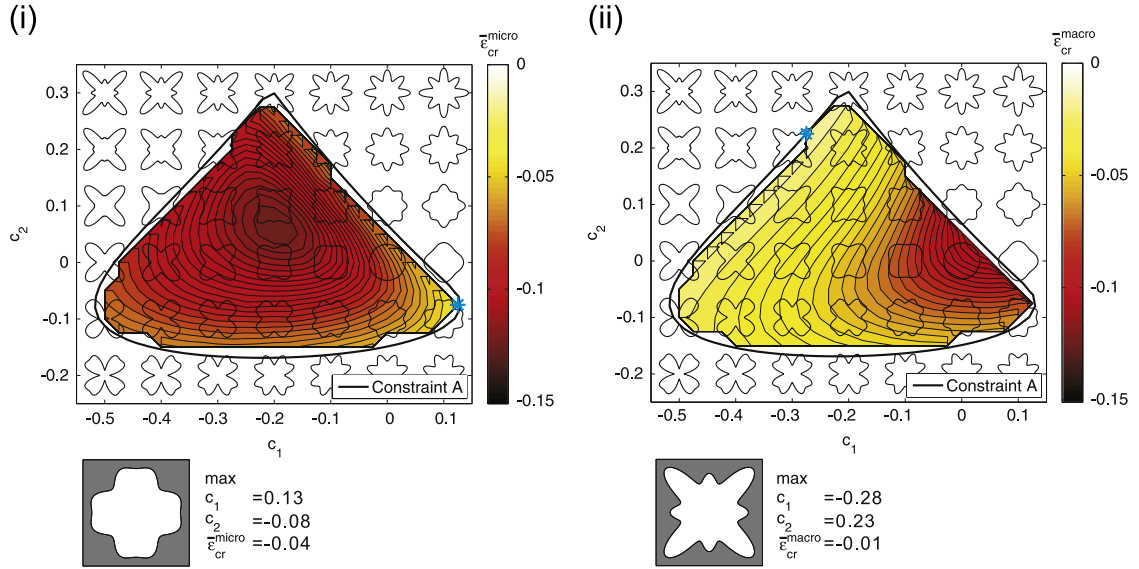
where f denotes min($\mathbb{L}_{ijkl}^H N_j N_l m_i m_k$) for the macroscopic instability analysis and the angular frequency ω for the microscopic instability analysis.

The results of the instability analyses are reported in Fig. 6 as contour maps, demonstrating that both $\bar{\varepsilon}_{cr}^{micro}$ and $\bar{\varepsilon}_{cr}^{macro}$ are significantly affected by the pore shape. The absolute value of $\bar{\varepsilon}_{cr}^{micro}$ is found to be minimum for pores characterized by a '+' shape (i.e. defined by positive values of c_1). In contrast, macroscopic instabilities are encountered very early along the loading path in the case of '×' shaped pores (i.e. defined by negative values of c_1), which accommodate compression by allowing a shear along one of the axes of the '×'.
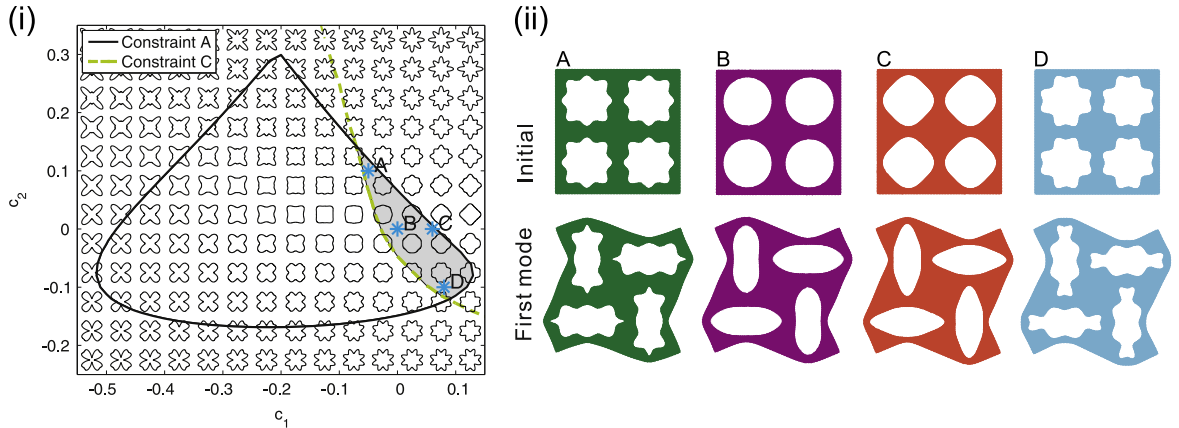
In this study we are interested in the post-buckling response of structures for which short wavelength instabilities are critical. For these structures

$$\bar{\varepsilon}_{cr}^{micro} - \bar{\varepsilon}_{cr}^{macro} \leq 0, \tag{30}$$

which will be referred to as *Constraint C*. In Fig. 7i both the boundaries for *Constraint A* and *Constraint C* are shown, enclosing

ARTICLE IN PRESS

J.T.B. Overvelde, K. Bertoldi / J. Mech. Phys. Solids ∎ (∎∎∎∎) ∎∎∎–∎∎∎ 9

Fig. 6. (i) Contour map showing the critical microscopic strain $\bar{\varepsilon}_{cr}^{micro}$ as a function of c_1 and c_2. (ii) Contour map showing the critical macroscopic strain $\bar{\varepsilon}_{cr}^{macro}$ as a function of c_1 and c_2.

Fig. 7. (i) *Constraint A* and *Constraint C* for $\phi_0 = 0.5$ and $\bar{t} = 0.15$. The domain for which microscopic instabilities are critical is enclosed by both curves and is highlighted in gray. (ii) Initial shapes and critical buckling modes for four representative structures.
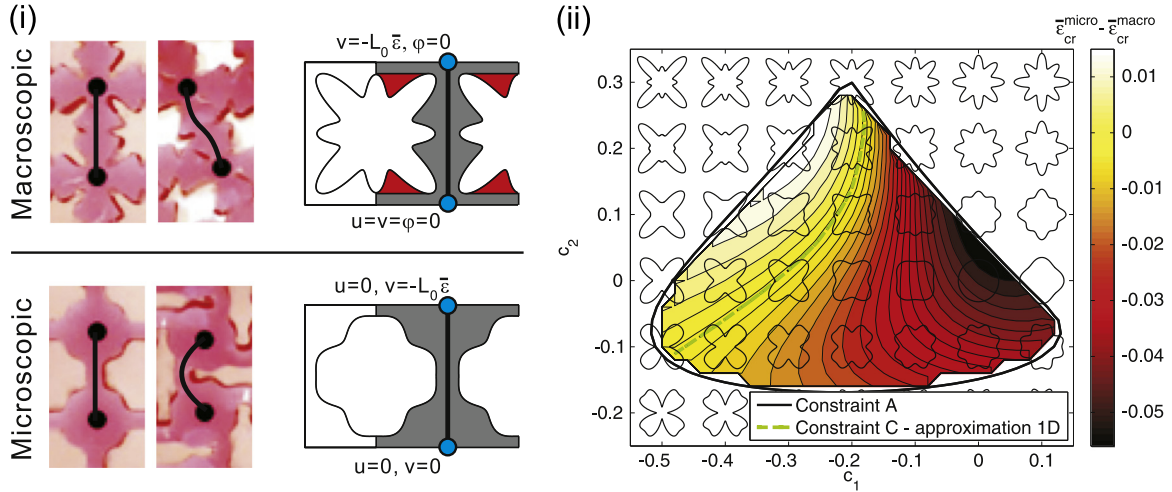
a feasible domain in which the structures undergo microscopic instability. Interestingly, our systematic study reveals that for pores characterized by a '+' shape *Constraint C* is satisfied and microscopic instabilities are critical. In contrast, for '×' shaped pores macroscopic instabilities are critical. For pores that show an equal contribution of '×' and '+' shape (i.e. $c_1 \sim 0$), the critical strains for microscopic and macroscopic instabilities are close to each other, so that a competition between the two types of instabilities is observed. Finally, we note that for all the structures that satisfy *Constraint C* the critical instability is characterized by a wavelength equal to $2L_0$ in both vertical and horizontal direction and leads to the formation of a checkerboard pattern, as shown in Fig. 7ii for four representative microstructures.

Next, to better understand how pore shape affects the wavelength of the critical instability, we focus on the deformation of the ligaments and model them as beams with varying cross-section along their length (see Fig. 8i). Since during the initial linear elastic regime the vertical ligaments of the porous structure are found to fully carry the uniaxial load (see Fig. 5), we start by considering only one vertical member (see Fig. 8i). Guided by both experiments and simulations (Overvelde et al., 2012), we identify the boundary conditions for the 1D beam model: for the case of microscopic instability we apply pin–pin boundary conditions (i.e. we set the transverse displacement $u=0$ at both ends); for the case of macroscopic instability we fix the rotation at both ends (i.e. $\phi = 0$) and the transverse displacement only at the lower end. We then determine the critical strain under uniaxial compression for both sets of boundary conditions performing finite-element simulations in ABAQUS/Standard. The beam is discretized using 100 linear beam elements (ABAQUS element type B21) and the critical strain is obtained through a linear buckling analysis (ABAQUS step type ∗BUCKLE). We consider beams with a cross-section corresponding to all pore shapes within the feasible $c_1 - c_2$ domain and determine the region in which microscopic

ARTICLE IN PRESS

10   J.T.B. Overvelde, K. Bertoldi / J. Mech. Phys. Solids ▮ (▮▮▮▮) ▮▮▮–▮▮▮
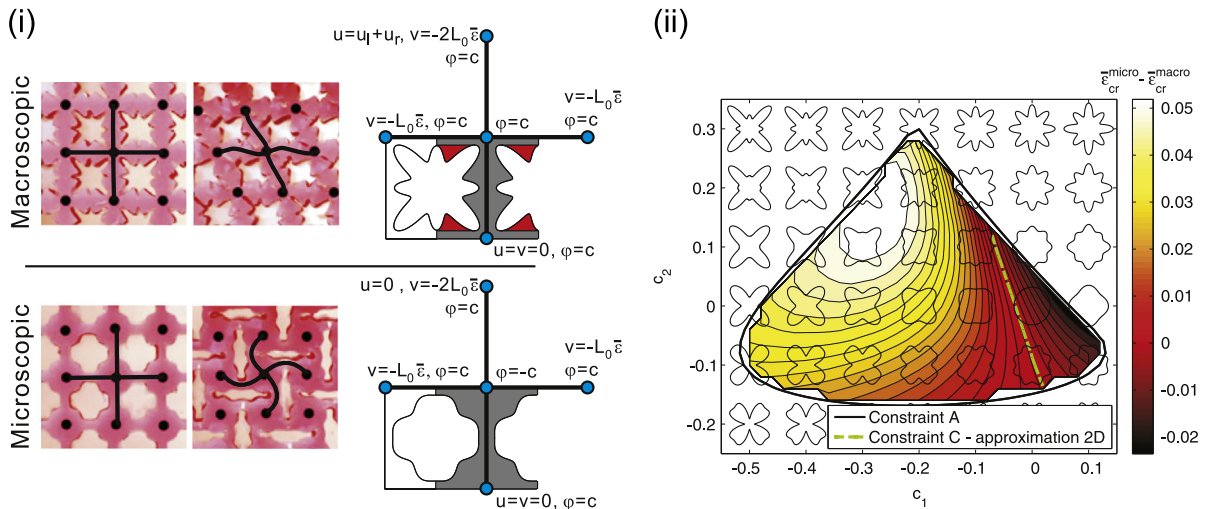
instabilities are critical. The boundary between microscopic and macroscopic modes predicted by the 1D model corresponds to the dashed line in Fig. 8ii, revealing that the simple beam model captures the essence of the problem, but does not predict the correct value for the critical strains. In particular, the 1D beam model underestimates the critical microscopic strain, leading to an enlarged region of structures that are characterized by a microscopic mode.
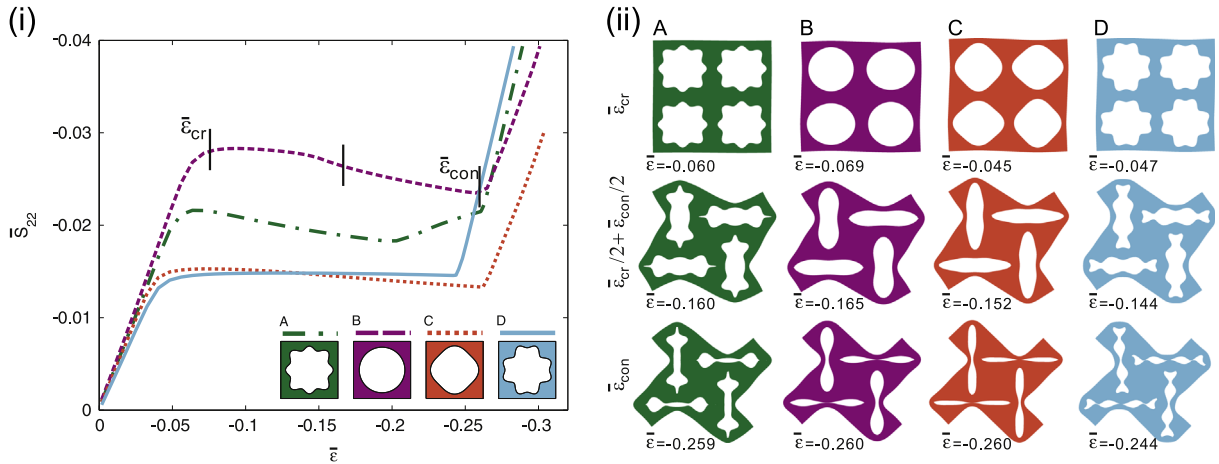
To improve the quantitative agreement with the 2D solid continuum models, we construct beam models comprising four beams characterized by the same cross-section used in the 1D beam models (see Fig. 9i). Periodic boundary conditions are applied to the four outer nodes, as shown in Fig. 9i. Moreover, to enforce microscopic instability the rotation of the center node is constrained to be opposite to that of the outer nodes. In contrast, for the macroscopic instability we equate the rotation of the center node to that of the outer nodes. As for the 1D model, a linear buckling analysis is conducted for both

Fig. 8. (i) Experimental images (Overvelde et al., 2012) showing the deformation under uniaxial compression of the vertical ligaments in porous samples undergoing macroscopic (top) and microscopic (bottom) instabilities. Based on these experimental images, 1D beam models are constructed. The beams have varying cross-section along their length and appropriate boundary conditions are applied. Here, L_0 is the size of the primitive cell, u and v correspond to the displacement of each node in horizontal and vertical direction, respectively, and φ is the rotational degree of freedom. (ii) Contour map showing $\overline{\varepsilon}_{cr}^{micro} - \overline{\varepsilon}_{cr}^{macro}$ as predicted by the 1D beam model as a function of c_1 and c_2. The dashed line corresponds to *Constraint C*.

Fig. 9. (i) Experimental images (Overvelde et al., 2012) showing the deformation under uniaxial compression of both the vertical and horizontal ligaments in porous samples undergoing macroscopic (top) and microscopic (bottom) instabilities. Based on these experimental images, 2D beam models are constructed. The beams have varying cross-section along their length and appropriate boundary conditions are applied. Here, L_0 is the size of the primitive cell, u and v correspond to the displacement of each node in horizontal and vertical direction, respectively, and φ is the rotational degree of freedom. The subscripts l and r indicate left and right nodes, respectively. (ii) Contour map showing $\overline{\varepsilon}_{cr}^{micro} - \overline{\varepsilon}_{cr}^{macro}$ as predicted by the 2D beam model as a function of c_1 and c_2. The dashed line corresponds to *Constraint C*.

ARTICLE IN PRESS

J.T.B. Overvelde, K. Bertoldi / J. Mech. Phys. Solids ∎ (∎∎∎∎) ∎∎∎–∎∎∎

11

Fig. 10. (i) Evolution of the macroscopic nominal stress $\overline{S}_{22}$ as a function of the macroscopic strain $\overline{\varepsilon}$ for four representative structures. (ii) Numerical images of the four representative structures at different levels of macroscopic strain: $\overline{\varepsilon}_{cr}$, $(\overline{\varepsilon}_{cr} + \overline{\varepsilon}_{con})/2$ and $\overline{\varepsilon}_{con}$, in which $\overline{\varepsilon}_{con}$ is the strain at which the pore faces come into self-contact.

sets of boundary conditions to calculate the value of *Constraint C*. The results are reported in Fig. 9ii as a contour map, where the color represents the value of *Constraint C*. This parametric study shows that the 2D beam model accurately estimates the region in which microscopic instabilities are critical (see the dashed line in Fig. 9ii). Therefore, our results clearly indicate that the horizontal ligaments play a crucial role in determining the wavelengths of the critical modes.

4.3. Post-buckling analysis

We now focus on the structures for which microscopic instabilities are critical (i.e. the structures that satisfy both *Constraint A* and *Constraint C*) and perform non-linear load–displacement analyses to capture their post-buckling deformation. First, we investigate the effect of pore shape on the stress–strain response and on the incremental modulus of the structures. Then, we focus on the effect of the pore shape on the evolution of the lateral strain. Since for all structures considered in this study the critical microscopic instability is characterized by a periodicity of 2×2, RVEs consisting of four primitive cells are used in the post-buckling analyses.
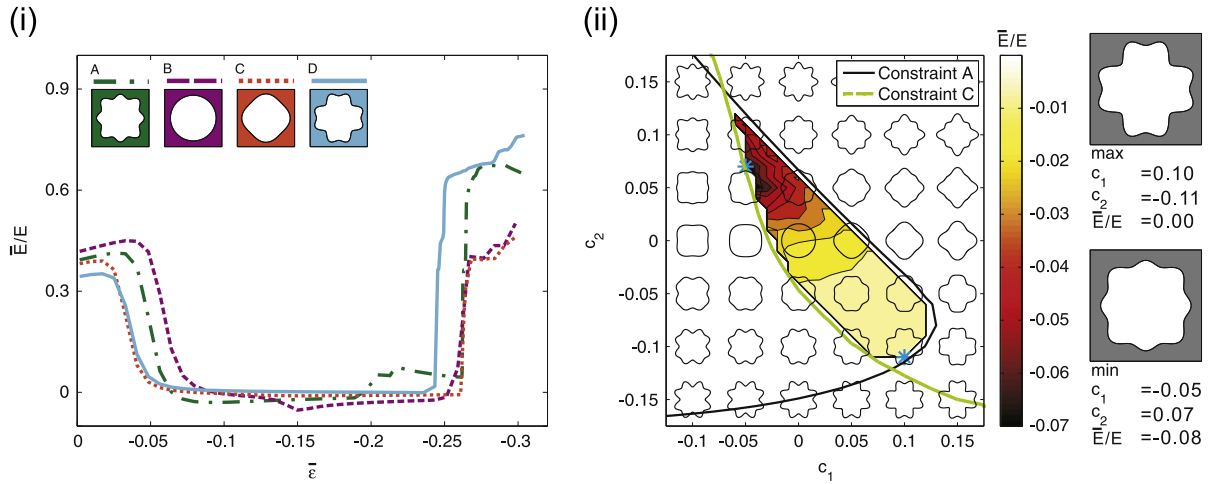
4.3.1. Stress–strain response

We start by focusing on the four representative structures A–D shown in Fig. 7ii. Fig. 10i shows the evolution of the macroscopic nominal stress $\overline{S}_{22}$ as a function of the applied engineering strain $\overline{\varepsilon}$. For all four structures we observe a behavior that is typical for cellular solids with three distinct regimes: a linear elastic regime, a stress plateau following thereafter and compaction by further compression. Images of the four configurations at different levels of deformation are reported in Fig. 10ii. First, we observe that when the critical value of the compressive strain is reached, buckling occurs, leading to the formation of a checkerboard pattern. Once formed, the new pattern becomes further accentuated for increased values of the applied strain. Finally, we notice that the non-linear response of all four representative structures is characterized by the same key features and the pore shape is found only to affect the strain at which transitions between the three different regimes occurs.

4.3.2. Incremental stiffness

Next, we focus on the evolution of the homogenized structural stiffness, defined as

$$\overline{E} = \frac{\partial \overline{S}_{22}}{\partial \overline{\varepsilon}}. \tag{31}$$

In Fig. 11i the evolution of the incremental stiffness as a function of $\overline{\varepsilon}$ is shown for the four representative structures A–D. The three regimes observed in the stress–strain response are clearly reflected in the evolution of $\overline{E}$, which is characterized by three distinct regions. The first region corresponds to the initial linear elastic stiffness $\overline{E}_0$ studied in Section 4.1. The second region plateaus at $\overline{E} \simeq 0$ and is observed after a sharp transition induced by the instability. To better understand the effect of pore shape on this plateau, in Fig. 11ii we report as a contour map the homogenized structural stiffness at $\overline{\varepsilon} = -0.1$ for all structures characterized by microscopic instability. The results clearly show that all structures are characterized by $\overline{E} \leq 0$. In particular, the minimum value of $\overline{E}$ (i.e. $\overline{E}/E = -0.08$) is found for almost square pores characterized by $(c_1, c_2) = (-0.05, 0.07)$.

ARTICLE IN PRESS

12   J.T.B. Overvelde, K. Bertoldi / J. Mech. Phys. Solids ∎ (∎∎∎∎) ∎∎∎–∎∎∎

Fig. 11. (i) Evolution of the macroscopic incremental stiffness $\bar{E}/E$ as a function of the macroscopic strain $\bar{\varepsilon}$ for four representative structures. (ii) Contour map of $\bar{E}/E$ at an applied strain $\bar{\varepsilon} = -0.1$ as a function of c_1 and c_2.

Finally, a sharp transition to $\bar{E} > 0$ occurs when the pores collapse. Although we stopped the simulations just after the point where contact occurs, we expect the structural stiffness for a completely collapsed structure to be approximately equal to that of the bulk material (i.e. $\bar{E}/E \simeq 1$).

4.3.3. Poisson's ratio

It has been recently demonstrated that microscopic instabilities strongly affect the evolution of the lateral strain, providing opportunities for the design of materials with tunable negative Poisson's ratio (Bertoldi et al., 2010). To quantify the lateral deformation of the porous structures, we define two Poisson's ratio-like quantities:

$$\bar{\nu}_{ref} = -\frac{\bar{\varepsilon}_{11}}{\bar{\varepsilon}} \quad \text{and} \quad \bar{\nu}_{def} = -\frac{\partial \bar{\varepsilon}_{11}}{\partial \bar{\varepsilon}}. \tag{32}$$
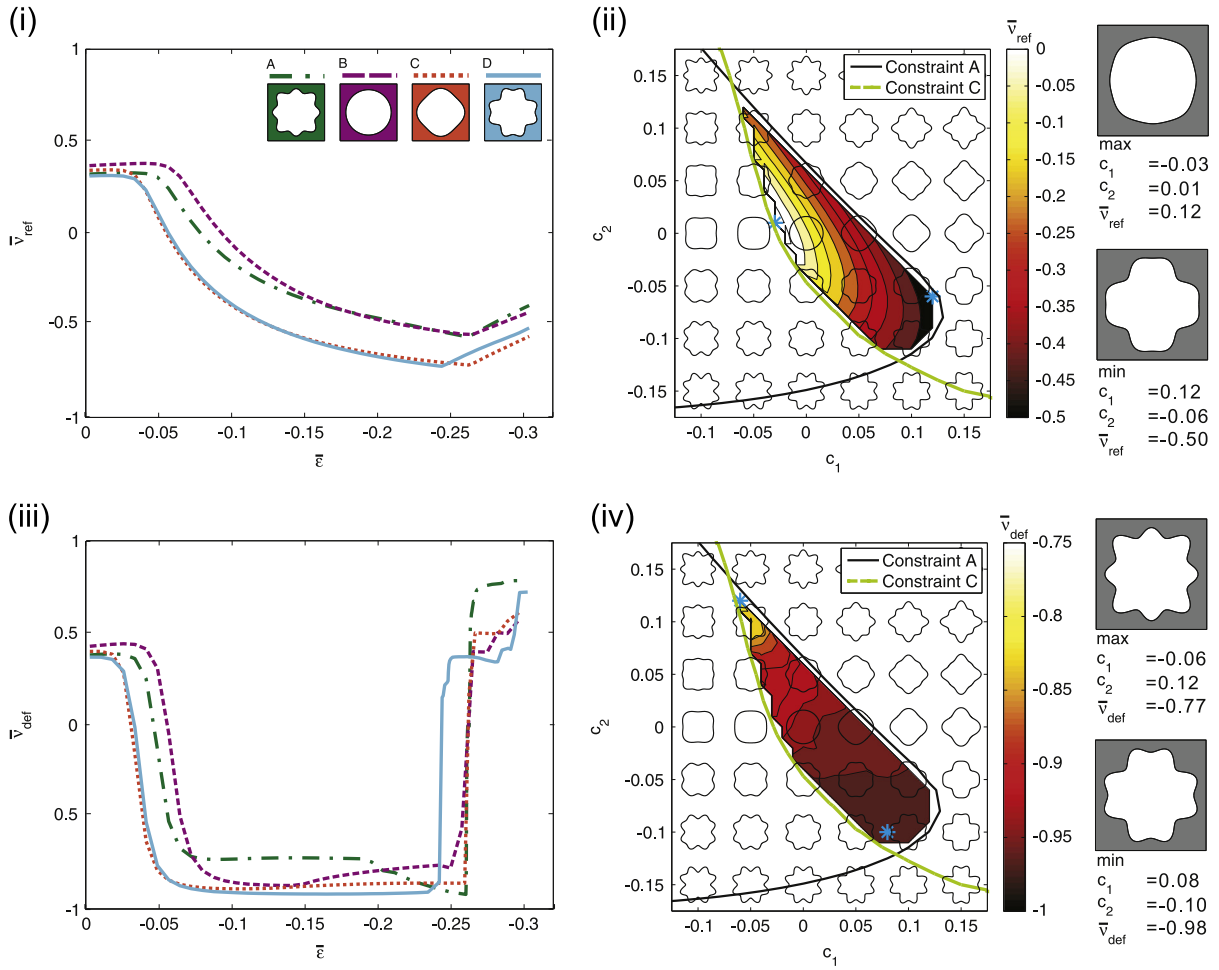
Note that $\bar{\nu}_{ref}$ characterizes the lateral deformation of the structure with respect to the undeformed configuration. Differently, $\bar{\nu}_{def}$ quantifies the lateral deformation with respect to the deformed configuration induced by an increment in the applied strain $\Delta\bar{\varepsilon}$ and allows us to describe Poisson's ratio of a material that operates around a pre-deformed state.

The evolution of $\bar{\nu}_{ref}$ and $\bar{\nu}_{def}$ as a function of the applied deformation for the four representative structures A–D is shown in Fig. 12i and iii, respectively. As expected, all structures are characterized by initially positive values of $\bar{\nu}_{ref}$ and $\bar{\nu}_{def}$. However, as previously observed for a square array of circular pores (Bertoldi et al., 2010), the dramatic pattern transformation introduced by instability strongly the Poisson's ratio of the structure. Beyond the instability, $\bar{\nu}_{ref}$ is found to monotonically decrease as a function of $\bar{\varepsilon}$ in all four structures and eventually becomes negative. While $\bar{\nu}_{ref}$ gradually decreases after instability, $\bar{\nu}_{def}$ is characterized by three plateaus. Before instability occurs, all structures are characterized by a constant and positive value of $\bar{\nu}_{def} \sim 0.4$. At instability, a rapid transition to a negative value close to -1 is observed. Finally, when the pores collapse due to large deformation and negative Poisson's ratio behavior, a sharp transition to a positive value $\bar{\nu}_{def} \sim 0.5$ is expected, since at this point we are left with a pre-stressed homogeneous solid that has the same properties as the bulk material.
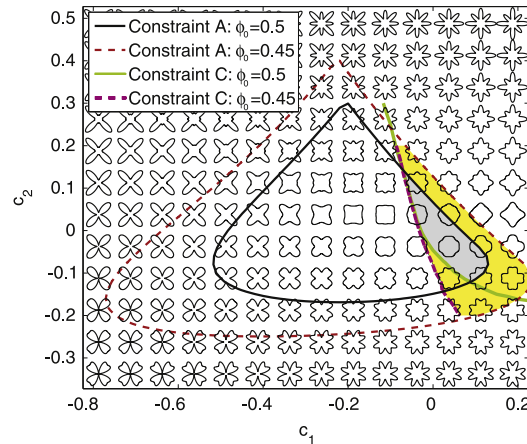
Next, we consider all structures for which microscopic instabilities are critical and calculate their Poisson's ratio $\bar{\nu}_{ref}$ and $\bar{\nu}_{def}$ at $\bar{\varepsilon} = -0.1$. The results are shown in Fig. 12ii and iv as a contour map, with the color representing the associated value of Poisson's ratio. The largest negative values for both $\bar{\nu}_{ref}$ and $\bar{\nu}_{def}$ are found for pores that are characterized by a '+' shape. For these pores microscopic instabilities are detected very early along the loading path, leading to a maximum lateral contraction. Moreover, our results indicate that circular pores do not lead to optimal compaction, instead an optimized folded configuration that maximizes the lateral contraction is found in structures with '+' shaped pores, demonstrating the significant effect that the pore shape has in the design of foldable soft structures.

5. Discussion and conclusion

In this study we numerically investigated the effect of pore shape on the non-linear response of a square array of pores in an elastomeric matrix. Our results show that the pore shape strongly affects structural stability, not only changing the critical strain, but most importantly the wavelength of the critical mode. In particular, our study reveals that only a limited number of pore shapes lead to periodic structures for which microscopic instabilities are critical. Focusing on structures characterized by 50% porosity, pores characterized by a '+' shape have the tendency to compress in the direction of the applied strain, leading to microscopic instabilities. In contrast, '×' shaped pores accommodate compression by allowing a shear along one of the axes of the '×', leading to macroscopic instabilities.

ARTICLE IN PRESS

J.T.B. Overvelde, K. Bertoldi / J. Mech. Phys. Solids ∎ (∎∎∎∎) ∎∎∎–∎∎∎   13

Fig. 12. (i) Evolution of the macroscopic Poisson's ratio with respect to the reference configuration $\overline{\nu}_{ref}$ as a function of the macroscopic strain $\overline{\varepsilon}$ for four representative structures. (ii) Contour map showing $\overline{\nu}_{ref}$ at an applied strain $\overline{\varepsilon} = -0.1$ as a function of c_1 and c_2. (iii) Evolution of the macroscopic Poisson's ratio with respect to the deformed configuration $\overline{\nu}_{def}$ as a function of the macroscopic strain $\overline{\varepsilon}$ for four representative structures. (iv) Contour map showing $\overline{\nu}_{def}$ at an applied strain $\overline{\varepsilon} = -0.1$ as a function of c_1 and c_2.

Fig. 13. Comparison of *Constraint A* and *Constraint C* for $\phi_0 = 0.5$ and $\phi_0 = 0.45$, considering $\overline{t} = t_{min}/L_0 = 0.15$. The domains in which microscopic instabilities are critical correspond to the gray highlighted region for $\phi_0 = 0.5$ and to both the gray and yellow regions for $\phi_0 = 0.45$. (For interpretation of the references to color in this figure caption, the reader is referred to the web version of this paper.)

ARTICLE IN PRESS

14   J.T.B. Overvelde, K. Bertoldi / J. Mech. Phys. Solids ▮ (▮▮▮▮) ▮▮▮–▮▮▮

In an effort to reduce the number of design variables and highlight the effect of pore shape, in this paper we present results for porous structures characterized by 50% initial porosity. However, the same numerical strategy can be applied to structures characterized by different levels of porosity. As an example, in Fig. 13 we compare the domains in which microscopic instabilities are critical for porous structures characterized by 50% and 45% initial porosity, considering $\bar{t} = t_{min}/L_0 = 0.15$. The domains in which microscopic instabilities are critical correspond to the gray highlighted region for $\phi_0 = 0.5$ and to both the gray and yellow regions for $\phi_0 = 0.45$. Therefore, the results indicate that a small reduction in porosity leads to a larger number of pore shapes for which microscopic instability is critical.
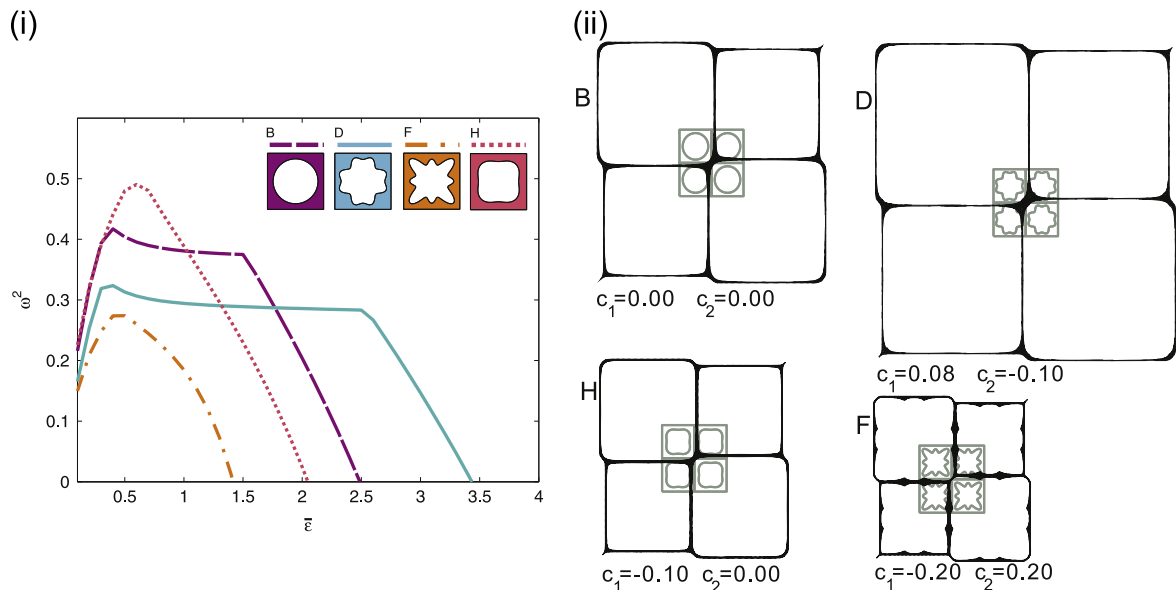
Although in this study we only focused on the non-linear response of the structures under uniaxial compression, we also expect that the pore shape significantly affects their behavior for different loading conditions. As an example, inspired by recent observations reported by Michel et al. (2007), we investigated the stability of the porous structures under equibiaxial tension, so that

$$\overline{\mathbf{F}} = (1+\bar{\varepsilon})\mathbf{e}_1 \otimes \mathbf{e}_1 + (1+\bar{\varepsilon})\mathbf{e}_2 \otimes \mathbf{e}_2 + \mathbf{e}_3 \otimes \mathbf{e}_3. \tag{33}$$

The results for four representative porous structures characterized by $\phi_0 = 0.50$ and $(c_1, c_2) = (0.00, 0.00)$, $(0.08, -0.10)$, $(-0.20, 0.20)$ and $(-0.10, 0.00)$ (corresponding to structures B, D, F and H in Fig. 5, respectively) are shown in Fig. 14. In Fig. 14i we report the evolution of the squared angular frequency ω^2 of a wave with wavelength equal to $2L_0$ along both lattice vectors as a function of the applied strain $\bar{\varepsilon}$. Initially all structures are characterized by positive values of ω^2, but for a critical value of the loading parameter we find that $\omega^2 = 0$, marking the onset of instability. Remarkably, the shape of the pores is found to significantly affect this onset. In particular, a very high critical strain occurs for pores characterized by a '+' shape (see pores B and D). In contrast, the instability is encountered much earlier along the loading path in the case of '×' shaped pores (see pores H and F). In particular, for the investigated shapes, the lowest critical strain is observed for shape F, which becomes unstable at $\bar{\varepsilon}_{cr}^F = 1.47$. Finally, in Fig. 14ii we show the critical mode superimposed on the deformed configuration at the onset of the instability, further highlighting the significant effect of pore shape on the critical strain. We note that all structures are characterized by a similar mode, leading to an alternation of pores with different sizes.

Interestingly, porous solids for which microscopic instabilities are critical open avenues for the design of reconfigurable and foldable structures. Unlike many other examples of foldable structures, our system does not contain rigid links, but only comprises a continuous distribution of soft material. Our structures take advantage of mechanical instabilities, allowing the actuation to be fast, reversible and applicable over a wide range of length scales. Our results demonstrate that by simply changing the shape of the pores, the response of porous structure can be easily tuned and soft structures with optimal compaction can be designed. Surprisingly, we show that circular pores do not lead to optimal response and that the compaction of the system can be significantly improved through a careful design of the pore shape. The insights gained by performing a numerical parametric exploration serve as an important design guideline in fabricating practical materials towards applications.

Finally, while it has been successfully shown that in the case of structures with linear response, topology optimization can be applied to find structures that exhibit extreme properties (Sigmund and Torquato, 1997; Sigmund, 1994, 1994; Schwerdtfeger et al., 2011; Sigmund and Søndergaard Jensen, 2003), the extension of these algorithms to highly non-linear

Fig. 14. (i) The evolution of the squared angular frequency ω^2 of a wave with wavelength equal to $2 L_0$ along both lattice vectors as a function of the applied strain $\bar{\varepsilon}$ for four representative porous structures (corresponding to structures B, D, F and H in Fig. 5). (ii) The critical mode for pore shapes B, D, F and H superimposed on the deformed configuration at the onset of the instability.

ARTICLE IN PRESS

J.T.B. Overvelde, K. Bertoldi / J. Mech. Phys. Solids ∎ (∎∎∎∎) ∎∎∎–∎∎∎ 15

problems still remains unresolved. The insights gained through this parametric study can be utilized to guide the design of structures with desired non-linear response. In terms of shape optimization, we have investigated the (c_1, c_2) design space. We have also defined constraints that enclose regions for which either microscopic or macroscopic buckling is critical. In these regions the macroscopic properties vary continuously as a function of the parameters (c_1, c_2). Therefore, our study provides a first important step toward the development of efficient topology optimization algorithms for highly non-linear problems.

Acknowledgments

References

Ashby, M., Bréchet, Y., 2003. Designing hybrid materials. Acta Mater. 51 (19), 5801–5821.

Aberg, M., Gudmundson, P., 1997. The usage of standard finite element codes for computation of dispersion relations in materials with periodic microstructure. J. Acoust. Soc. Am. 102 (4), 2007–2013.

Bertoldi, K., Boyce, M., Deschanel, S., Prange, S., Mullin, T., 2008. Mechanics of deformation-triggered pattern transformations and superelastic behavior in periodic elastomeric structures. J. Mech. Phys. Solids 56, 2642–2668.

Bertoldi, K., Reis, P.M., Willshaw, S., Mullin, T., 2010. Negative Poisson's ratio behavior induced by an elastic instability. Adv. Mater. 22 (3), 361–366.

Bertoldi, K., Reis, P., Willshaw, S., Mullin, T., 2010. Negative Poisson's ratio behavior induced by an elastic instability. Adv. Mater. 22, 361–366.

Chan, E., Smith, E., Hayward, R., Crosby, A., 2008. Surface wrinkles for smart adhesion. Adv. Mater. 20 (4), 711–716.

Chung, J., Waas, A.M., 2002. Compressive response of circular cell polycarbonate honeycombs under in plane biaxial static and dynamic loading. Part I. Experiments. Int. J. Impact Eng. 27 (7), 729–754.

Chung, J.Y., Youngblood, J.P., Stafford, C.M., 2007. Anisotropic wetting on tunable micro-wrinkled surfaces. Soft Matter 3, 1163–1169.

Danielsson, M., Parks, D., Boyce, M., 2002. Three-dimensional micromechanical modeling of voided polymeric materials. J. Mech. Phys. Solids 50 (2), 351–379.

Evans, A., Hutchinson, J., Fleck, N., Ashby, M., Wadley, H., 2001. The topological design of multifunctional cellular metals. Prog. Mater. Sci. 46, 309–327.

Forterre, Y., Skotheim, J., Dumais, J., Mahadevan, L.L., 2005. How the venus flytrap snaps. Nature 433, 421–425.

Geymonat, G., Müller, S., Triantafyllidis, N., 1993. Homogenization of nonlinearly elastic materials, microscopic bifurcation and macroscopic loss of rank-one convexity. Arch. Ration. Mech. Anal. 122, 231–290.

Gibson, L., Ashby, M., 1999. Cellular Solids: Structure and Properties. Cambridge University Press.

Jang, J., Koh, C.Y., Bertoldi, K., Boyce, M.C., Thomas, E.L., 2009. Combining pattern instability and shape-memory hysteresis for phononic switching. Nano Lett. 9 (5), 2113–2119.

Khare, K., Zhou, J., Yang, S., 2009. Tunable open-channel microfluidics on soft poly(dimethylsiloxane) (pdms) substrates with sinusoidal grooves. Langmuir 25 (21), 12794–12799.

Krishnan, D., Johnson, H., 2009. Optical properties of two-dimensional polymer photonic crystals after deformation-induced pattern transformations. J. Mech. Phys. Solids 57 (9), 1500–1513.

Lee, H., Xia, C., Fang, N.X., 2010. First jump of microgel; actuation speed enhancement by elastic instability. Soft Matter 6, 4342–4345.

Li, J., Shim, J., Deng, J., Overvelde, J.T.B., Zhu, X., Bertoldi, K., Yang, S., 2012. Switching periodic membranes via pattern transformation and shape memory effect. Soft Matter 8, 10322–10328.

Michel, J.C., Lopez-Pamies, O., Casta neda, P.P., Triantafyllidis, N., 2007. Microscopic and macroscopic instabilities in finitely strained porous elastomers. J. Mech. Phys. Solids 55 (5), 900–938.

Mullin, T., Deschanel, S., Bertoldi, K., Boyce, M.C., 2007. Pattern transformation triggered by deformation. Phys. Rev. Lett. 99, 084301.

Ogden, R.W., 1998. Nonlinear Elastic Deformations. Dover, New York.

Ohno, N., Okumura, D., Noguchi, H., 2002. Microscopic symmetric bifurcation condition of cellular solids based on a homogenization theory of finite deformation. J. Mech. Phys. Solids 50 (5), 1125–1153.

Overvelde, J.T.B., Shan, S., Bertoldi, K., 2012. Compaction through buckling in 2D periodic, soft and porous structures: effect of pore shape. Adv. Mater. 24 (17), 2337–2342.

Papka, S.D., Kyriakides, S., 1994. In-plane compressive response and crushing of honeycomb. J. Mech. Phys. Solids 42 (10), 1499–1532.

Papka, S., Kyriakides, S., 1998. Experiments and full-scale numerical simulations of in-plane crushing of a honeycomb. Acta Mater. 35 (8), 2765–2776.

Queheillalt, D.T., Wadley, H.N., 2005. Cellular metal lattices with hollow trusses. Acta Mater. 53 (2), 303–313.

Rogers, J.A., Someya, T., Huang, Y., 2010. Materials and mechanics for stretchable electronics. Science 327 (5973), 1603–1607.

Schwerdtfeger, J., Wein, F., Leugering, G., Singer, R.F., Körner, C., Stingl, M., Schury, F., 2011. Design of auxetic structures via mathematical optimization. Adv. Mater. 23 (22–23), 2650–2654.

Shim, J., Shan, S., Kosmrlj, A., Kang, S.H., Chen, E.R., Weaver, J.C., Bertoldi, K., 2013. Harnessing instabilities for design of soft reconfigurable auxetic/chiral materials. Soft Matter 9, 8198–8202.

Sigmund, O., 1994. Materials with prescribed constitutive parameters: an inverse homogenization problem. Int. J. Solids Struct. 31 (17), 2313–2329.

Sigmund, O., Søndergaard Jensen, J., 2003. Systematic design of phononic band-gap materials and structures by topology optimization. Philos. Trans. R. Soc. Lond. A 361 (1806), 1001–1019.

Sigmund, O., Torquato, S., 1997. Design of materials with extreme thermal expansion using a three-phase topology optimization method. J. Mech. Phys. Solids 45 (6), 1037–1067.

Shim, J., Perdigou, C., Chen, E.R., Bertoldi, K., Reis, P.M., 2012. Buckling-induced encapsulation of structured elastic shells under pressure. Proc. Natl. Acad. Sci. 109 (16), 5978–5983.

Sigmund, O., 1994. Design of Material Structures Using Topology Optimization (Ph.D. thesis). Technical University of Denmark, December 1994.

Steele, C., 2000. Shell stability related to pattern formation in plants. J. Appl. Mech. 67, 237–247.

Tantikom, K., Aizawa, T., Mukai, T., 2005. Symmetric and asymmetric deformation transition in the regularly cell-structured materials. Part II. Theoretical study. Int. J. Solids Struct. 42 (8), 2211–2224.

Triantafyllidis, N., Schraad, M.W., 1998. Onset of failure in aluminum honeycombs under general in-plane loading. J. Mech. Phys. Solids 46 (6), 1089–1124.

Triantafyllidis, N., Nestorovic, M.D., Schraad, M.W., 2006. Failure surfaces for finitely strained two-phase periodic solids under general in-plane loading. J. Appl. Mech. 73, 505–515.

ARTICLE IN PRESS

16   J.T.B. Overvelde, K. Bertoldi / J. Mech. Phys. Solids ▮ (▮▮▮▮) ▮▮▮–▮▮▮

Verdejo, R., Stämpfli, R., Alvarez-Lainez, M., Mourad, S., Rodriguez-Perez, M., Brühwiler, P., Shaffer, M., 2009. Enhanced acoustic damping in flexible polyurethane foams filled with carbon nanotubes. Compos. Sci. Technol. 69 (10), 1564–1569.

Wadley, H., 2006. Multifunctional periodic cellular metals. Philos. Trans. R. Soc. A 364 (1838), 31–68.

Wierzbicki, T., Abramowicz, N., 1983. On the crushing mechanics of thin-walled structures. J. Appl. Mech. 50, 727–734.

Yin, J., Cao, Z., Li, C., Sheinman, I., Chen, X., 2008. Stress-driven buckling patterns in spheroidal core/shell structures. Proc. Natl. Acad. Sci. 105 (49), 19132–19135.

Yoo, P., Suh, K., Park, S., Lee, H., 2002. Physical self-assembly of microstructures by anisotropic buckling. Adv. Mater. 14 (19), 1383–1387.

Zhang, Y., Matsumoto, E.A., Peter, A., Lin, P., Kamien, R.D., Yang, S., 2008. One-step nanoscale assembly of complex structures via harnessing of an elastic instability. Nano Lett. 8 (4), 1192–1196.